

DFTR: Depth-supervised Hierarchical Feature Fusion Transformer for Salient Object Detection

Heqin Zhu^{1,2} Xu Sun²✉ Yuexiang Li² Kai Ma² S. Kevin Zhou^{1,3}✉
Yefeng Zheng²

¹Key Lab of Intelligent Information Processing of Chinese Academy of Sciences (CAS),
Institute of Computing Technology, CAS, Beijing 100190, China

²Tencent JARVIS Lab, Shenzhen, China

³School of Biomedical Engineering & Suzhou Institute for Advanced Research,
Center for Medical Imaging, Robotics, and Analytic Computing & Learning (MIRACLE),
University of Science and Technology of China, Suzhou 215123, China

ericxsun@tencent.com

Abstract

Automated salient object detection (SOD) plays an increasingly crucial role in many computer vision applications. Although existing frameworks achieve impressive SOD performances especially with the development of deep learning techniques, their performances still have room for improvement. In this work, we propose a novel pure Transformer-based SOD framework, namely Depth-supervised hierarchical feature Fusion TRansformer (DFTR), to further improve the accuracy of both RGB and RGB-D SOD. The proposed DFTR involves three primary improvements: 1) The backbone of feature encoder is switched from a convolutional neural network to a Swin Transformer for more effective feature extraction; 2) We propose a multi-scale feature aggregation (MFA) module to fully exploit the multi-scale features encoded by the Swin Transformer in a coarse-to-fine manner; 3) Following recent studies, we formulate an auxiliary task of depth map prediction and use the ground-truth depth maps as extra supervision signals for network learning. To enable bidirectional information flow between saliency and depth branches, a novel multi-task feature fusion (MFF) module is integrated into our DFTR. We extensively evaluate the proposed DFTR on ten benchmarking datasets. Experimental results show that our DFTR consistently outperforms the existing state-of-the-art methods for both RGB and RGB-D SOD tasks. The code and model will be released.

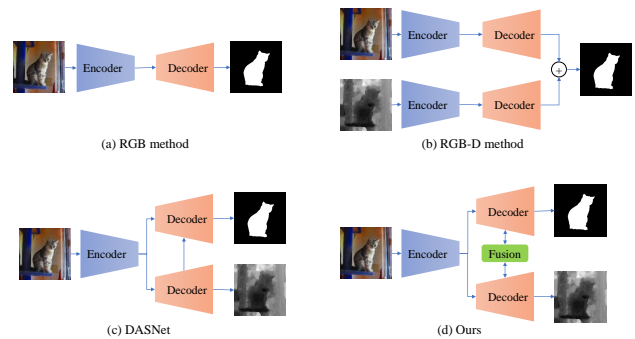


Figure 1. Different kinds of SOD frameworks. (a) Typical RGB-based: with RGB as the only input. (b) Typical RGB-D-based: with both RGB and depth as inputs. (c) DASNet [63]: with RGB as input and depth as supervision, decoding information only feeds from the depth map recovery branch to the salient object segmentation branch. (d) Ours: with RGB as input and depth as supervision, a multi-task feature fusion module is further developed to enable bidirectional information flow between saliency and depth decoders. We name frameworks (c) and (d) as depth-supervised RGB (RGB-DS) SOD methods.

1. Introduction

Salient object detection (SOD), which aims to detect and segment the most noticeable objects in a scene, is a fundamental task for various computer vision applications, such as semantic segmentation [26], image translation [23] and visual tracking [25]. At the very beginning of this area, previous methods only took the RGB image as input (Fig. 1 (a)). For example, Zhao *et al.* [66] proposed a pyramid feature attention network that generates saliency maps. Al-

¹Xu Sun and S. Kevin Zhou are the corresponding authors.

though the RGB-based approaches are simple and easy-to-implement, they often fail to tackle images with complex backgrounds.

To address the problem, researchers attempted to integrate the depth information into SOD frameworks as complementary guidance for object detection. As shown in Fig. 1 (b), most RGB-D frameworks deployed two streams to extract useful features from RGB and depth images, respectively, and then fused the features for the plausible saliency results. For example, Han *et al.* [19] proposed a two-stream network to extract features from RGB and depth images, respectively, and then fuse them with a combination layer. Zhao *et al.* [64] implemented a feature-enhancement module and fluid pyramid integration module for the better fusion of RGB and depth features. Owing to the auxiliary depth information, the accuracy of SOD task gains a significant increase. However, recent study revealed the main drawbacks of RGB-D methods: 1) the additional depth branch increases the computational cost and 2) the paired depth maps are usually unavailable in real applications.

To deal with previously mentioned challenges, Zhao *et al.* [63] formulated a new research line for SOD by proposing a unified framework (namely DASNet), which only takes the depth maps as supervision at training stage. The pipeline of DASNet is presented in Fig. 1 (c). Concretely, the DASNet took only RGB images as input and simultaneously output the predictions of salient object segmentation and depth map reconstruction. The auxiliary information learned from the depth map recovery task was adopted to regularize the features for salient object segmentation and thereby boost the SOD performance. Compared to the dual-stream RGB-D approach, the DASNet, consisting of one encoder and two decoders, remarkably decreases the computational cost. Nevertheless, we argue that there is still an improvement space for the architecture of this unified framework: 1) The importance of flexible information flow has been verified for deep learning framework by existing studies [20, 21, 65]. To this end, the single-direction regularization (*i.e.*, from depth map recovery to salient object segmentation) degrades the information transmission between the two decoders. 2) The modules of DASNet (*e.g.* channel-aware fusion module) are all based on vanilla convolutional neural network (CNN). Recently, vision Transformers (ViT) [11] have shown their superiority to CNN on a variety of computer vision tasks, but few studies introduced ViT into the area of SOD.

In this paper, we propose a pure Transformer network, namely **Depth-supervised Hierarchical Feature Fusion TRansformer (DFTR)**, which is in an encoder-decoder architecture. Similar to DASNet [63], our DFTR has an encoder and a two-stream decoder for salient object detection and depth map prediction, respectively. The depth maps are used as the supervision signal during RGB-DS learn-

ing [63]. Differently, the proposed DFTR adopts Swin Transformer [33] as the backbone for encoder to effectively extract discriminative features, and its decoder consists of two novel modules (*i.e.*, multi-scale feature aggregation (MFA) and multi-task feature fusion (MFF) modules) for the dense high-resolution prediction. The former module aggregates features from the adjacent scales, while the latter one improves the flexibility of information flow between the branches of two-stream decoder. In summary, our contributions can be categorized into three folds:

- We propose a pure Transformer network, termed DFTR, for accurate salient object detection. The proposed DFTR adopts the RGB-DS learning strategy; hence, only RGB image is required at inference stage for both RGB and RGB-D SOD tasks.
- Two novel modules (MFA and MFF) are developed to better fuse features extracted from adjacent scales and different decoder branches, respectively. Both of them are based on Transformer for effective feature extraction and fusion.
- The proposed DFTR framework is evaluated on multiple publicly available SOD benchmarking datasets. The experimental results validate the effectiveness of our DFTR—a new state-of-the-art SOD performance is achieved.

2. Related Work

2.1. Transformer

Due to the self-attention mechanism, Transformer can effectively model long-range dependencies and extract global context features. In recent years, Transformer has shown the superiority to convolutional neural network (CNN) in various computer vision tasks, *e.g.* image classification [4, 11, 58], object detection [3, 46], and image segmentation [49, 53, 69]. A variety of pure Transformer backbone networks without convolutional operations have been proposed. For example, T2T-ViT [57] incorporates a layer-wise Tokens-to-Token (T2T) transformation with a deep-narrow efficient backbone to simultaneously reduce token length and extract rich local features. The Swin Transformer [33] decreases the time complexity of self-attention computation from $\mathcal{O}(N^2)$ to $\mathcal{O}(N)$ by limiting the areas for self-attention computation (*i.e.*, a local window). Such a local window will be shifted across the whole image to capture the global context.

2.2. Salient Object Detection

CNN-based SOD Methods. For RGB SOD and RGB-D SOD tasks, various CNN-based methods [13, 14, 16, 17, 38, 50, 54, 61–63, 67, 68] have been proposed in recent years,

which are superior to traditional methods [9, 10, 15, 18, 48, 72] based on hand-crafted features. Most CNN-based RGB SOD methods [14, 17, 38, 54, 62, 63] adopt the encoder-decoder architecture. Commonly, the encoder uses a pre-trained network (*e.g.*, ResNet [20] and VGG [47]) as backbone, while the decoder is an elaborately designed network. For examples, Zhang *et al.* [59] proposed the first uncertainty model, which has a generative architecture to learn from data labeling process. Fu *et al.* [16] developed a Siamese network to jointly learn saliency map and depth map. A novel densely cooperative fusion (DCF) module was proposed to extract complementary features. Tang *et al.* [50] disentangled the SOD task into a low-resolution saliency classification task and a high-resolution refinement regression task. Furthermore, several studies [14, 41, 67] integrated the spatial and channel attention mechanism to the decoder for SOD performance improvement. Most existing CNN-based RGB-D SOD methods mainly focus on the fusion (*e.g.* summation, multiplication or concatenation) of RGB and depth features [5, 6, 16] or the utilization of depth map [21, 28, 41, 64].

Transformer-based SOD Methods. Until now, there are only two Transformer-based SOD methods, termed visual saliency Transformer (VST) [32] and TriTransNet [34]. The VST [32] proposed by Liu *et al.* was the first pure Transformer method for SOD task, which adopts T2T-ViT [57] as backbone network. Concretely, the VST leveraged multi-level token fusion and adopted a new token upsampling method to yield high-resolution detection results. TriTransNet [34] had a triplet Transformer embedding module to capture long-range dependencies across layers. In particular, the encoders of triplet Transformer module share weights for multi-level feature enhancement, while the three-stream decoder is individually initialized for multi-modal fusion. Both the previously mentioned Transformer-based methods achieved satisfactory SOD performances, *i.e.*, outperforming the state-of-the-art CNN-based approaches, which validate the effectiveness of Transformer structure.

Different from VST [32], our DFTR adopts the powerful Swin Transformer [33] as the backbone for encoder. Furthermore, we propose an elaborately designed multi-scale feature aggregation module for the decoder, which progressively aggregates hierarchical features on two adjacent levels from low-resolution to high-resolution and finally generates the SOD map. For better feature fusion, a multi-task feature fusion (MFF) module, enhancing the information flow between saliency and depth branches, is implemented. Taking the spatial correlation between RGB image and depth map, our MFF module fuses features along the channel-wise dimension. Such a design is computational-efficiency, compared to the existing TransFuser [43] that

spatially fuses RGB and LiDAR features.

3. Methodology

We present a novel Transformer-based neural network for RGB-D and RGB salient object detection tasks, named as Depth-supervised Hierarchical Feature Fusion TRansformer (DFTR). As Figure 2 shows, our proposed DFTR model takes an encoder-decoder architecture. The encoder is a Transformer network based on Swin Transformer [33] for feature extraction, described in Section 3.1. The decoder is of a dual-stream structure for multi-task learning (here one for saliency prediction and the other for depth estimation), consisting of a multi-scale feature aggregation (MFA) module in Section 3.2 and a multi-task feature fusion (MFF) module in Section 3.3. The MFA module simultaneously aggregates multi-scale features extracted from encoder from high-level to low-level while the MFF module connects multiple tasks by fusing features from different task branches. The overall architecture is demonstrated in Section 3.4 and the learning objective is in Section 3.5.

3.1. Transformer Encoder

3.1.1 Swin Transformer Block

Swin Transformer [33] mainly consists of Transformer blocks [51] in which the standard multi-head self-attention (MSA) module is replaced by a shifted window-based module. In detail, a Swin Transformer block is composed of a shifted window multi-head self-attention module (SW-MSA), followed by a two-layer MLP with GELU activation. A LayerNorm (LN) layer is adopted before each SW-MSA and each MLP, and a residual shortcut is adopted behind each module. In this paper, we also adopt Swin Transformer block to build the MFA and MFF modules, which are described in Sections 3.2 and 3.3, respectively.

Different from standard Transformer architecture which conducts global self-attention, Swin Transformer only performs self-attention within non-overlapping local windows for efficient modeling and rapid computation. To enable cross-window connections and enhance long-range dependencies, a shifted window partitioning approach is further introduced to shift neighboring non-overlapping window partition between consecutive Swin Transformer blocks,

3.1.2 Hierarchical Feature Extraction

Swin Transformer produces four scales of hierarchical feature maps at four stages by starting from small-sized image patches and gradually merging neighboring patches in deeper layers. First, the input RGB image is partitioned into non-overlapping patches of size 4×4 , resulting in

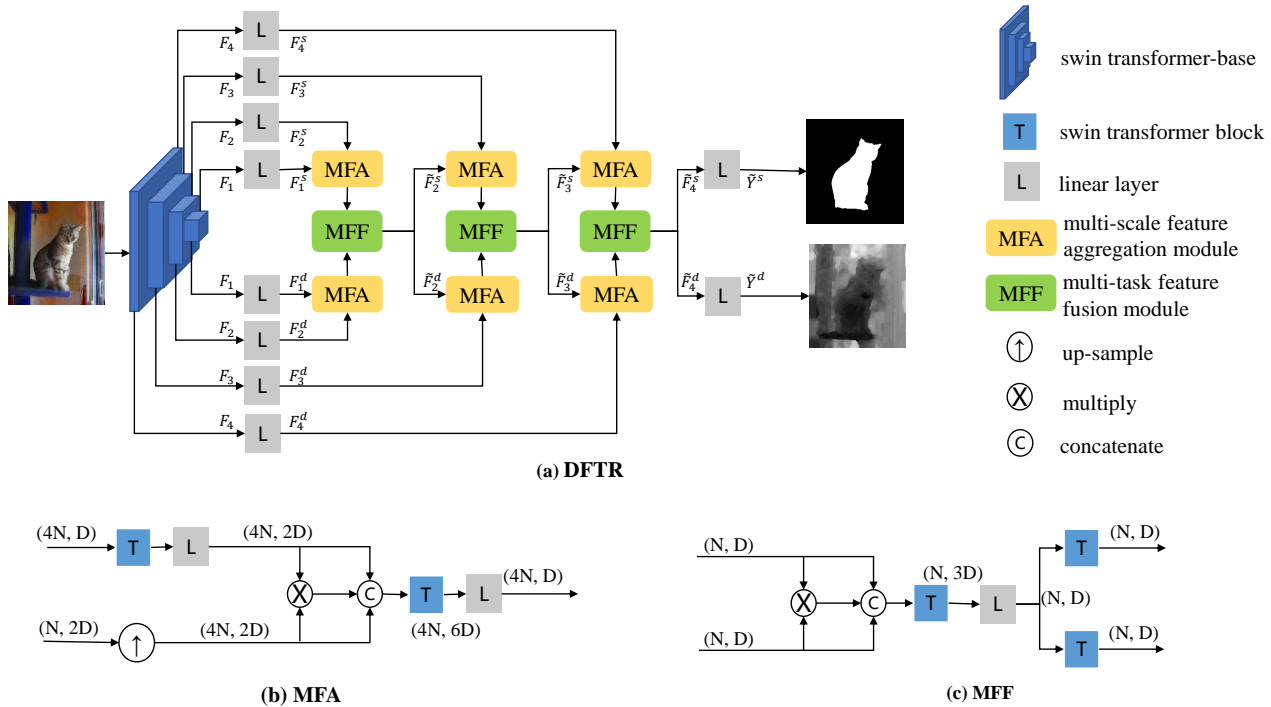


Figure 2. (a) Overview of the network structure of DFTR which consists of a Swin Transformer encoder backbone and two hierarchical decoding branches for saliency detection and depth estimation, respectively. (b) MFA: Multi-scale feature aggregation module. (c) MFF: Multi-task feature fusion module.

$4 \times 4 \times 3 = 48$ feature dimensions for each patch. A linear embedding layer is then employed to project this raw-valued feature into an arbitrary dimension (denoted as C), forming patch tokens in a shape of $(\frac{H}{4} \times \frac{W}{4}, C)$. These patch tokens are then fed into several consecutive Swin Transformer blocks, with the number of tokens remaining as $\frac{H}{4} \times \frac{W}{4}$. The whole procedure mentioned above is referred to as ‘‘Stage 1’’.

To generate a hierarchical representation in the successive stage, patches are merged by concatenating each group of 2×2 neighboring patches and then converted to high-dimension patches by a linear layer. Let N denote the number of input tokens and D denote the input dimension, the output shape of the patch merging layers becomes $(\frac{N}{4}, 2D)$. Similar to Stage 1, a sequence of Swin Transformer blocks is applied to the merged patches at each following stage, while keeping the number of tokens unchanged. For Swin Transformer base model, the numbers of Swin Transformer blocks at each stage are 2, 2, 18, and 2, respectively. Finally, four levels of hierarchical feature maps, denoted as F_4 , F_3 , F_2 and F_1 , are generated from the Swin Transformer backbone with shapes being $(\frac{H}{4} \times \frac{W}{4}, C)$, $(\frac{H}{8} \times \frac{W}{8}, 2C)$, $(\frac{H}{16} \times \frac{W}{16}, 4C)$, and $(\frac{H}{32} \times \frac{W}{32}, 8C)$, respectively.

3.2. Multi-scale Feature Aggregation Module

The Swin Transformer encoder produces hierarchical feature maps of different spatial resolutions, but introduces large semantic gaps caused by different learning stages. The high-resolution maps have low-level features that are very useful for accurate positioning yet harm their representational power for salient object detection. In contrast, low-resolution maps have high-level features which are semantically strong yet easily blur the boundary of the salient object. In order to make full use of the low-level and high-level features for accurate dense prediction, we design a multi-scale feature aggregation (MFA) module that gradually aggregates features of different scales, with a similar form like FCN [35] and U-Net [44].

Figure 2 (b) shows the building blocks that construct our MFA module. Taking a coarse-resolution feature map and a high-resolution feature map as inputs, MFA module seeks to expand them into the same shape at first. More specifically, the spatial dimension of the coarse-resolution feature maps f_1^{in} is upsampled by a factor of 2 using bilinear interpolation to generate feature maps f_1^{mid} in shape of $(4N, 2D)$, while the channel dimension of the high-resolution feature maps f_2^{in} is enlarged by a factor of 2 through a Swin Transformer block and a linear layer to obtain feature maps f_2^{mid}

in shape of $(4N, 2D)$. Inspired by DASNet [63], we then multiply f_1^{mid} and f_2^{mid} element-wisely to form a new feature map f^{mul} to enhance common pixels and alleviate ambiguous pixels. Next, we concatenate f_1^{mid} , f_2^{mid} and f^{mul} channel-wisely to get the aggregated feature map f^{cat} in shape of $(4N, 6D)$. The above procedure is summarized as:

$$f^{\text{cat}} = U(f_1^{\text{in}}) \odot L_{\theta_2}(T_{\theta_1}(f_2^{\text{in}})) \odot (U(f_1^{\text{in}}) \otimes L_{\theta_2}(T_{\theta_1}(f_2^{\text{in}}))), \quad (1)$$

where \odot represents concatenation; \otimes represents element-wise multiplication; U, T, L represent upsample, Swin Transformer block and linear layer, respectively; θ_i with $i \in \{1, 2, 3, 4\}$ represents different learning parameters that correspond to a Swin Transformer block or a linear layer. A ReLU activation is employed after each linear layer.

Finally, we use a Swin Transformer block to aggregate concatenated features and a linear layer to perform channel dimension reduction. The final output feature maps f^{out} are formulated as:

$$f^{\text{out}} = L_{\theta_4}(T_{\theta_3}(f^{\text{cat}})). \quad (2)$$

3.3. Multi-task Feature Fusion Module

Unlike most previous frameworks which employ a two-stream feature extraction network to respectively generate hierarchical features from depth maps and RGB images, we adopt a multi-task learning strategy to jointly perform depth estimation and saliency detection. Taking depth map as a supervised constraint at training stage allows the network to take only RGB images as inputs, and meanwhile combine depth prior knowledge with learned parameters. This is desirable for real-world applications as the paired depth maps are usually unavailable in real industrial setups.

To enable bidirectional information transmission between two decoding branches, we further design a novel multi-task feature fusion (MFF) module that fuses saliency feature map and depth feature map in same scales. As illustrated in Figure 2 (c), the MFF module tends to fuse two types of source feature maps, namely, $f_1^{\text{in}} \in R^{N \times D}$ from the saliency branch and $f_2^{\text{in}} \in R^{N \times D}$ from the depth branch, into $f_1^{\text{out}} \in R^{N \times D}$ and $f_2^{\text{out}} \in R^{N \times D}$. Specifically, element-wise multiplication is first performed on f_1^{in} and f_2^{in} to enhance the common features. The enhanced feature map f^{mul} is then concatenated with the source features to obtain $f^{\text{cat}} \in R^{N \times 3D}$. To further fuse the concatenated feature map, a Swin Transformer block is applied, followed by a linear layer for channel reduction. The fused feature map f^{fuse} is formulated as:

$$f^{\text{fuse}} = L_{\theta_2}(T_{\theta_1}(f_1^{\text{in}} \odot f_2^{\text{in}} \odot (f_1^{\text{in}} \otimes f_2^{\text{in}}))). \quad (3)$$

For the outputs of different tasks, we assign each task a Swin Transformer block to generate task-specific feature map from the fused feature map, which is represented as:

$$f_1^{\text{out}} = T_{\theta_3}(f^{\text{fuse}}), \quad f_2^{\text{out}} = T_{\theta_4}(f^{\text{fuse}}). \quad (4)$$

Note that our MFF module concatenates feature maps from different tasks in channel dimension to leverage the spatial relevance between saliency maps and depth maps, which is different from TransFuser [43] that spatially fuses features maps from two modality domains.

3.4. Overview of DFTR

As illustrated in Figure 2 (a), the encoded multi-scale feature maps $[F_4, F_3, F_2, F_1]$ are first passed through linear layers for channel reduction. Specifically, two groups of linear layers are employed for two decoding branches separately: one for saliency detection and the other for depth estimation. This procedure can be defined as:

$$F_i^s = L_{\theta_i}^s(F_i), \quad F_i^d = L_{\theta_i}^d(F_i), \quad (5)$$

where s represents saliency, d denotes depth, and $i \in \{1, 2, 3, 4\}$ indicates the i -th level.

For each branch, three MFA modules are adopted sequentially to aggregate four levels of hierarchical features in a coarse-to-fine manner. An MFF module is inserted at each level to fuse the outputs of MFA modules from both depth and saliency decoders. The fused feature maps are then fed into the successive MFA modules. We summarize these operations as follows:

$$\begin{aligned} \tilde{F}_1^s &= F_1^s; \quad \tilde{F}_1^d = F_1^d, \\ Z_{i+1}^s &= \text{MFA}_{\theta_i}^s(\tilde{F}_i^s, F_{i+1}^s), \\ Z_{i+1}^d &= \text{MFA}_{\theta_i}^d(\tilde{F}_i^d, F_{i+1}^d), \\ \tilde{F}_{i+1}^s, \tilde{F}_{i+1}^d &= \text{MFF}_{\theta_i}(Z_{i+1}^s, Z_{i+1}^d). \end{aligned} \quad (6)$$

where $i \in \{1, 2, 3\}$. Finally, we use linear layers to obtain the prediction maps \tilde{Y}^s and \tilde{Y}^d , which is formulated as:

$$\tilde{Y}^s = L_{\theta_{\text{final}}}^s(\tilde{F}_4^s), \quad \tilde{Y}^d = L_{\theta_{\text{final}}}^d(\tilde{F}_4^d). \quad (7)$$

3.5. Learning Objective

Following [63], we train our network with three objectives, as illustrated in Figure 3. To be specific, we use binary cross entropy (BCE) and intersection over union (IOU) loss functions for SOD supervision and log mean squared error (logMSE) for depth supervision. Besides, a depth error-weighted correction (DEC) loss [63] is further adopted to mine ambiguous pixels by leveraging the depth prediction mistakes. Three levels of intermediate saliency feature maps $\tilde{F}_2^s, \tilde{F}_3^s, \tilde{F}_4^s$ and the final prediction Y^s are used for multi-level supervision (MLS). The overall loss is given as:

$$\mathcal{L} = \mathcal{L}_{\text{logMSE}} + \sum_{i=1}^4 \lambda_i (\mathcal{L}_{\text{BCE}} + \mathcal{L}_{\text{IOU}} + \mathcal{L}_{\text{DEC}}), \quad (8)$$

where λ_i 's are the loss weights of different levels and empirically set to $[0.4, 0.6, 0.8, 1.0]$.

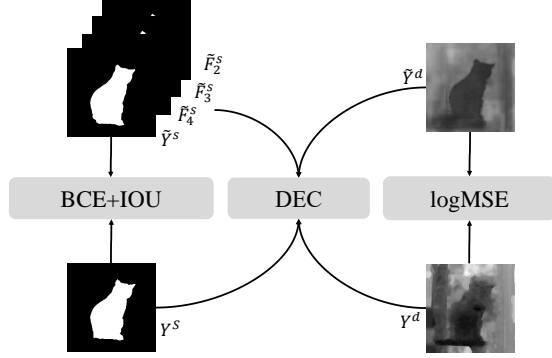


Figure 3. An illustration of the relationships of loss functions between the predictions and ground truth labels. The DEC loss is error-weighted BCE loss from DASNet [63]. \tilde{Y}^s, \tilde{Y}^d are predicted saliency and depth maps, respectively, while Y^s, Y^d are corresponding ground truth labels. We use additional supervision signals with saliency maps $\tilde{F}_2^s, \tilde{F}_3^s, \tilde{F}_4^s$ which are the outputs of MFF modules for multi-level supervision (MLS).

4. Experiments

4.1. Experimental Settings

Datasets. For RGB-D SOD, we adopt five publicly available datasets for performance evaluation, which are NJU2K [24] (1,985 images), STERE [37] (1,000 images), NLPR [39] (1,000 images), SSD [71] (80 images), and SIP [13] (929 images). Concretely, we train SOD models with a set, consisting of 1,500 NJU2K images and 700 NLPR images. All the rest images of five benchmarking datasets are adopted for testing.

For RGB SOD, we conduct experiments on five widely-used datasets, *i.e.*, DUTS [52] (15,572 images), ECSSD [55] (1,000 images), DUT-OMRON [56] (5,168 images), PASCAL-S [30] (850 images), and HKU-IS [29] (4,447 images). Similarly, SOD models are trained with 10,553 images from the public train-set of DUTS, and tested on the rest images of the five datasets. To generate the depth images of DUTS dataset for the training of our DFTR, we adopt Adabins [2], a state-of-the-art method, for depth estimation.

Evaluation Metrics. For quantitative evaluation, we adopt four metrics to evaluate the performance of our model. Specifically, **structure measure** (S_α) [7] is used to evaluate region-aware and object-aware structural similarity; **maximum F-measure** (F_β) [1] is the weighted harmonic mean of precision and recall; **maximum enhanced-alignment measure** (E_ξ) [12] jointly captures image-level statistics and local pixel matching information; **mean absolute error** (M) [40] evaluates the pixel-wise error between predictions and the ground truth.

Implementation Details. The proposed DFTR is implemented using PyTorch. The model is trained with an NVIDIA Tesla V100 GPU (version 11).² We adopt the Swin Transformer pre-trained on ImageNet [45] as the backbone of encoder. At training stage, we resize each image to 352×352 pixels and adopt random horizontal flipping, random cropping, and multi-scale resizing for data augmentation. The SGD optimizer is deployed for network optimization. The maximum learning rate is 0.002 for backbone and 0.02 for other parts, which cyclically varies from zero to maximum and then from maximum to zero. The batch size is set to 16. Our model is observed to converge after 200 epochs of training. At testing stage, the image is first resized to 352×352 pixels and then fed into our model to yield the predicted saliency map, which is finally rescaled back to the original size for SOD performance evaluation.

4.2. Comparisons with State-of-the-art Methods

RGB-D SOD comparison. We involve 6 traditional methods, 16 CNN-based methods and 2 newly developed Transformer-based methods (TriTransNet [34] and VST [32]) for performance comparison. The SOD performances of different SOTA approaches and our DFTR are presented in Table 1. It can be observed that our DFTR achieves the best SOD performances under most metrics on different datasets. Especially, on NLPR and SSD datasets, our DFTR consistently outperforms all the listed benchmarking frameworks, which validates its superiority. Our DFTR outperforms Transformer-based methods (*i.e.*, VST and TriTransNet) on 16 of 20 metrics, while the rest 4 metrics are slightly worse than VST and TriTransNet. The underlying reason is that those approaches adopt depth maps as the auxiliary input to assist salient object detection. In contrast, the proposed DFTR relaxes the requirement of depth maps for model inference, and only takes the RGB images as input. We further visualize the saliency maps predicted by our model and other methods for qualitative comparison. As illustrated in Figure 4, our DFTR generates more accurate and clearer saliency maps compared to other methods.

RGB SOD comparison. Eight state-of-the-art methods, *i.e.*, ITSD-R [70], MINet-R [38], LDF-R [54], CSF-R2 [17], GateNet-R [67], DASNet [63], DH [32], and VST [32], are included for comparison in this experiment. The evaluation results are shown in Table 2. Similar trend of performance improvement to RGB-D-based comparison is observed. Particularly, our DFTR surpasses the state-of-the-art methods on most metrics (except F_β on DUT-OMRON and HKU-IS, and S_α on PASCAL-S). We further visualize the saliency maps predicted by our model and other methods for qualitative comparison. As illustrated in Figure 4,

²The code will be released soon after paper acceptance.

Table 1. Quantitative comparison of the proposed DFTR method with 24 **RGB-D SOD** models (including 6 traditional models, 16 deep CNN-based models and 2 Transformer-based models) on 5 public RGB-D saliency benchmark datasets in terms of 4 widely used evaluation metrics (*i.e.*, structure measure S_α [7], maximum F-measure F_β [1], maximum enhanced alignment measure E_ξ [12], and mean absolute error M [40]). “↑” (or “↓”) indicates that larger (or smaller) is better. The subscript of each model denotes the publication year. In each column, the best result is marked with **red** and the second best with **blue**.

Model	NJU2K [24]				STERE [37]				NLPR [39]				SSD [71]				SIP [13]			
	S_α ↑	F_β ↑	E_ξ ↑	M ↓	S_α ↑	F_β ↑	E_ξ ↑	M ↓	S_α ↑	F_β ↑	E_ξ ↑	M ↓	S_α ↑	F_β ↑	E_ξ ↑	M ↓	S_α ↑	F_β ↑	E_ξ ↑	M ↓
LBE ₁₆ [15]	.695	.748	.803	.153	.660	.633	.787	.250	.762	.745	.855	.081	.621	.619	.736	.278	.727	.751	.853	.200
DCMC ₁₆ [10]	.686	.715	.799	.172	.731	.740	.819	.148	.707	.666	.773	.111	.704	.711	.786	.169	.683	.618	.743	.186
SE ₁₆ [18]	.664	.748	.813	.169	.708	.755	.846	.143	.756	.713	.847	.091	.675	.710	.800	.165	.628	.661	.771	.164
MDSF ₁₇ [48]	.748	.775	.838	.157	.728	.719	.809	.176	.805	.793	.885	.095	.673	.703	.779	.192	.717	.698	.798	.167
CDCP ₁₇ [72]	.669	.621	.741	.180	.713	.664	.786	.149	.669	.621	.741	.180	.603	.535	.700	.214	.595	.505	.721	.224
DTM ₂₀ [9]	.706	.716	.799	.190	.747	.743	.837	.168	.733	.677	.833	.145	.677	.651	.773	.199	.690	.659	.778	.203
ICNet ₂₀ [28]	.894	.891	.926	.052	.903	.898	.942	.045	.923	.908	.952	.028	.848	.841	.902	.064	.854	.857	.903	.069
S ² MA ₂₀ [31]	.894	.889	.930	.053	.890	.882	.932	.051	.915	.902	.953	.030	.868	.848	.909	.052	.872	.877	.919	.057
A2dele ₂₀ [42]	.871	.874	.916	.051	.878	.879	.928	.044	.898	.882	.944	.029	.802	.776	.861	.070	.828	.833	.889	.070
SSF ₂₀ [60]	.899	.896	.935	.043	.893	.890	.936	.044	.914	.896	.953	.026	.845	.824	.897	.058	.876	.882	.922	.052
UCNet ₂₀ [59]	.897	.895	.936	.043	.903	.899	.944	.039	.920	.903	.956	.025	.865	.854	.907	.049	.875	.879	.919	.051
Cas-GNN ₂₀ [36]	.911	.903	.933	.035	.899	.901	.930	.039	.919	.904	.947	.028	.872	.862	.915	.047	.875	.879	.919	.051
CMMS ₂₀ [27]	.900	.897	.936	.044	.895	.893	.939	.043	.915	.896	.949	.027	.874	.864	.922	.046	.872	.877	.911	.058
CoNet ₂₀ [22]	.895	.893	.937	.046	.908	.905	.949	.040	.908	.887	.945	.031	.853	.840	.915	.059	.858	.867	.913	.063
DANet ₂₀ [68]	.899	.910	.935	.045	.901	.892	.937	.043	.915	.916	.953	.028	.864	.866	.914	.050	.875	.892	.918	.054
DASNet ₂₀ [63]	.902	.902	.939	.042	.910	.904	.944	.037	.929	.922	.964	.021	.885	.872	.930	.042	.877	.886	.925	.051
BBS-Net ₂₀ [14]	.921	.920	.949	.035	.908	.903	.942	.041	.930	.918	.961	.023	.882	.859	.919	.044	.879	.883	.922	.055
D ³ Net ₂₁ [13]	.900	.900	.950	.041	.899	.891	.938	.046	.912	.897	.953	.030	.857	.834	.910	.058	.860	.861	.909	.063
JLDCF ₂₁ [16]	.911	.913	.948	.040	.911	.907	.949	.039	.926	.917	.964	.023	-	-	-	-	.892	.900	.949	.046
DFMNet ₂₁ [61]	.906	.910	.947	.042	.898	.893	.941	.045	.923	.908	.957	.026	-	-	-	-	.883	.887	.926	.051
RD3D ₂₁ [8]	.916	.914	.947	.036	.911	.906	.947	.037	.930	.919	.965	.022	-	-	-	-	.885	.889	.924	.048
BTSNet ₂₁ [62]	.921	.924	.954	.036	.915	.911	.949	.038	.934	.923	.965	.023	-	-	-	-	.896	.901	.933	.044
TriTransNet ₂₁ [34]	.920	.919	.960	.020	.908	.893	.927	.033	.928	.909	.960	.020	-	-	-	-	.886	.892	.924	.043
VST ₂₁ [32]	.922	.920	.951	.035	.913	.907	.951	.038	.932	.920	.962	.024	.889	.876	.935	.045	.904	.915	.944	.040
DFTR (Ours)	.922	.923	.954	.034	.918	.914	.951	.034	.941	.934	.972	.018	.890	.882	.937	.036	.904	.913	.946	.040

Table 2. Quantitative comparison of our DFTR with 8 state-of-the-art **RGB SOD** methods on 5 public RGB saliency benchmark datasets under 4 measurements (*i.e.*, structure measure S_α [7], maximum F-measure F_β [1], maximum enhanced alignment measure E_ξ [12], and mean absolute error M [40]). “↑” (or “↓”) indicates that larger (or smaller) is better. The subscript of each model denotes the publication year. In each column, the best result is marked with **red** and the second best with **blue**.

Model	ECSSD [55]				DUTS [52]				DUT-OMRON [56]				HKU-IS [29]				PASCAL-S [30]			
	S_α ↑	F_β ↑	E_ξ ↑	M ↓	S_α ↑	F_β ↑	E_ξ ↑	M ↓	S_α ↑	F_β ↑	E_ξ ↑	M ↓	S_α ↑	F_β ↑	E_ξ ↑	M ↓	S_α ↑	F_β ↑	E_ξ ↑	M ↓
ITSD-R ₂₀ [70]	.925	.938	.957	.034	.885	.867	.929	.041	.840	.792	.880	.061	.917	.926	.960	.031	.861	.839	.889	.071
MINet-R ₂₀ [38]	.925	.938	.957	.034	.884	.864	.926	.037	.833	.769	.869	.056	.919	.926	.960	.029	.856	.831	.883	.071
LDf-R ₂₀ [54]	.925	.938	.954	.034	.892	.877	.930	.034	.839	.782	.870	.052	.920	.929	.958	.028	.861	.839	.888	.067
CSF-R ₂₀ [17]	.931	.942	.960	.033	.890	.869	.929	.037	.838	.775	.869	.055	-	-	-	-	.863	.839	.885	.073
GateNet-R ₂₀ [67]	.924	.935	.955	.038	.891	.874	.932	.038	.840	.782	.878	.055	.921	.926	.959	.031	.863	.836	.886	.071
DASNet ₂₀ [63]	.927	.950	-	.032	.894	.896	-	.034	.845	.827	-	.050	.922	.942	-	.027	.885	.849	-	.064
DH ₂₁ [50]	-	-	-	-	.892	.900	-	.035	.843	.820	-	.048	.922	.944	-	.026	-	-	-	-
VST ₂₁ [32]	.932	.944	.964	.034	.896	.877	.939	.037	.850	.800	.888	.058	.928	.937	.968	.030	.873	.850	.900	.067
DFTR (Ours)	.935	.949	.966	.028	.909	.900	.952	.029	.860	.812	.895	.046	.930	.941	.970	.025	.879	.878	.924	.054

our DFTR predicts more accurate saliency maps, validating the superiority of our model to other methods for salient object detection.

4.3. Ablation Study

We conduct an ablation study to investigate the contribution made by different components of the proposed DFTR to SOD accuracy. It is worthwhile to mention that models under different settings are trained with the same protocol stated in Sec. 4.1, and evaluated on NJU2K [24] and NLPR [39] datasets with the four metrics. The evaluation

results are presented in Table 3.

MFA Module. As shown in Table 3, model (a), using Swin Transformer and MLP as the encoder and decoder, respectively, is adopted as the baseline. Here, (a) is an RGB-based SOD model. By switching the decoder from MLP to our multi-scale feature aggregation (MFA) module (*i.e.*, model (b)), the SOD accuracies on NJU2K and NLPR test sets are observed to significantly increase, which demonstrates the effectiveness of aggregating the information of

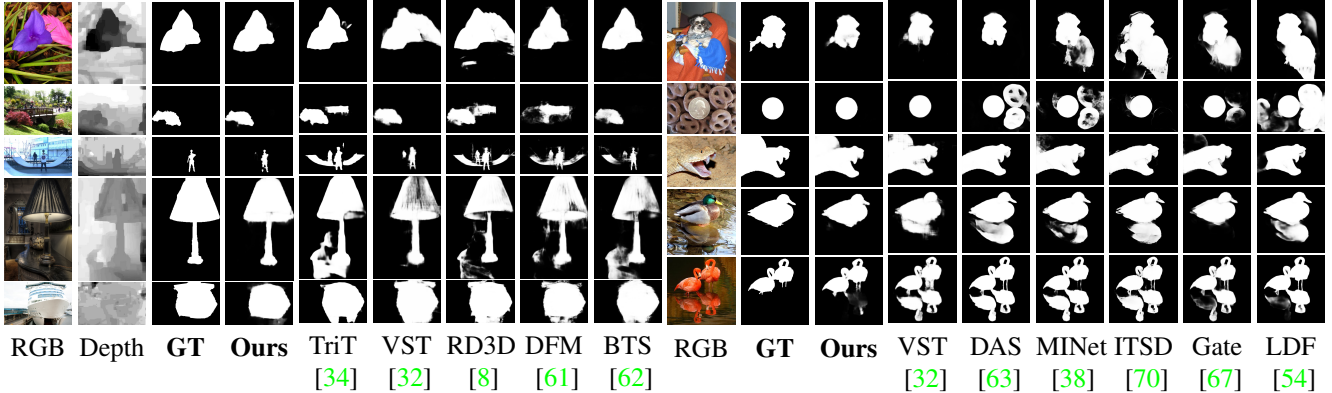


Figure 4. Qualitative comparison of our proposed method against the state-of-the-art **RGB-D** (left) and **RGB** (right) SOD methods.

Table 3. Ablation study of different components of our DFTR. “Swin” denotes Swin Transformer and “MLP” is a two-layer linear layer with GELU activation. “MFA (single)” represents only saliency branch is trained. “MLS” represents multi-level supervision. “MFA” and “MFF” are our proposed modules. We take **model (e)** as our final model. The best results are marked in **red**.

Index	Model	NJU2K [13]				NLPR [39]			
		$S_\alpha \uparrow$	$F_\beta \uparrow$	$E_\xi \uparrow$	$M \downarrow$	$S_\alpha \uparrow$	$F_\beta \uparrow$	$E_\xi \uparrow$	$M \downarrow$
(a)	Swin+MLP	.869	.863	.926	.066	.883	.848	.947	.040
(b)	Swin+MFA (single)	.916	.919	.951	.937	.935	.931	.968	.022
(c)	Swin+MFA	.919	.923	.953	.036	.937	.932	.971	.020
(d)	Swin+MFA+MLS	.920	.921	.953	.035	.939	.933	.970	.019
(e)	Swin+MFA+MLS+MFF	.922	.923	.954	.034	.941	.934	.972	.018

multi-scale features for SOD.

Multi-task Learning. As previously mentioned, model (b) is an RGB-based framework. To evaluate the contribution of multi-task learning (*i.e.*, SOD and depth map prediction), we implement a multi-task framework (model (c)) by integrating the depth map prediction branch into model (b). The decoder for depth map prediction is the same as the SOD branch. Due to the extra information provided by the depth map prediction task, the SOD performance of model (c) consistently surpasses that of model (b) as shown in Table 3.

Multi-level Supervision (MLS). To validate the effectiveness of multi-level supervision (MLS) strategy adopted for the decoder, we construct model (d) by adding MLS to model (c). It can be observed from Table 3 that the SOD performance is boosted by the use of MLS under most metrics (except F_β on NJU2K and E_ξ on NLPR).

Multi-task Feature Fusion (MFF) Module. To better fuse the features extracted from multi-tasks, we propose a multi-task feature fusion (MFF) module. Based on model (d), we integrate MFF modules between saliency MFA and

Table 4. Quantitative comparison with different hyper-parameter settings of our proposed DFTR model. In the table, “depth” represents the depth of each Swin Transformer block in the MFA and MFF module, while “down” represents the ratio of input dimension and output dimension of linear layers in Equation 5. We take **setting (b)** as our final setting. **Red** denotes the best results.

Index	Setting	NJU2K [13]				NLPR [39]			
		$S_\alpha \uparrow$	$F_\beta \uparrow$	$E_\xi \uparrow$	$M \downarrow$	$S_\alpha \uparrow$	$F_\beta \uparrow$	$E_\xi \uparrow$	$M \downarrow$
(a)	depth=2, down=8	.918	.920	.951	.038	.938	.933	.970	.019
(b)	depth=1, down=8	.922	.923	.954	.034	.941	.934	.972	.018
(c)	depth=1, down=4	.918	.920	.952	.037	.937	.930	.967	.021
(d)	depth=1, down=16	.921	.924	.955	.034	.939	.933	.971	.018

depth MFA modules, as shown in Fig. 2, which forms our final model (e). Such a module facilitates the information flow between different branches. As Table 3 shows, model (e) yields the best results under all metrics, which demonstrates the effectiveness of our MFF module for feature fusion. In summary, the above quantitative analysis shows the effectiveness of different components of our model. Our model is capable of integrating and fusing multi-task multi-scale features and makes accurate dense SOD predictions.

Evaluation on Hyper-parameters of DFTR Apart from different modules and strategies adopted in our DFTR, the setting of hyper-parameters is also an important factor, which may affect the model performance. To this end, we conduct an experiment to evaluate the model performance with different hyper-parameter settings.

The “depth” and “down” are two main hyper-parameters of our DFTR. Concretely, “depth” $\in \{1, 2\}$ represents the depth of Swin Transformer block adopted by MFA and MFF modules and “down” $\in \{4, 8, 16\}$ represents the ratio of input dimension and output dimension of linear layers in Equation (5). The evaluation results are presented in Table 4. As shown, setting (b), *i.e.*, depth=1 and down=8, reaches the best results with most metrics, which indicates the effectiveness of the linear layer for channel dimensional

reduction. Besides, the 1-depth Swin Transformer block is able to learn local features without shifting windows.

5. Conclusion

We rethought the importance of flexible information flow between saliency branch and depth branch for depth-supervised saliency detection and developed a pure Transformer network DFTR that works for both RGB and RGB-D SOD tasks. The decoder of DFTR consists of an MFA module that gradually aggregates multi-scale features from coarse to fine and an MFF module that fuses saliency and depth features bidirectionally to enhance the multi-task information transmission. Quantitative and qualitative results on RGB and RGB-D SOD demonstrated the effectiveness of our DFTR. With only RGB inputs at inference stage, our DFTR detects salient objects more accurately than any other CNN-based method or Transformer-based method.

References

- [1] Radhakrishna Achanta, Sheila Hemami, Francisco Estrada, and Sabine Susstrunk. Frequency-tuned salient region detection. In *CVPR*, pages 1597–1604. IEEE, 2009. 6, 7
- [2] Shariq Farooq Bhat, Ibraheem Alhashim, and Peter Wonka. Adabins: Depth estimation using adaptive bins. In *CVPR*, pages 4009–4018, 2021. 6
- [3] Nicolas Carion, Francisco Massa, Gabriel Synnaeve, Nicolas Usunier, Alexander Kirillov, and Sergey Zagoruyko. End-to-end object detection with transformers. In *ECCV*, pages 213–229. Springer, 2020. 2
- [4] Chun-Fu (Richard) Chen, Quanfu Fan, and Rameswar Panda. CrossViT: Cross-attention multi-scale vision transformer for image classification. In *ICCV*, pages 357–366, 2021. 2
- [5] Hao Chen and Youfu Li. Progressively complementarity-aware fusion network for RGB-D salient object detection. In *CVPR*, pages 3051–3060, 2018. 3
- [6] Hao Chen and Youfu Li. Three-stream attention-aware network for RGB-D salient object detection. *IEEE TIP*, 28(6):2825–2835, 2019. 3
- [7] Ming-Ming Chen and Deng-Ping Fan. Structure-measure: A new way to evaluate foreground maps. *IJCV*, 129:2622–2638, 2021. 6, 7
- [8] Qian Chen, Ze Liu, Yi Zhang, Keren Fu, Qijun Zhao, and Hongwei Du. RGB-D salient object detection via 3D convolutional neural networks. In *AAAI*, volume 35, pages 1063–1071, 2021. 7, 8
- [9] Runmin Cong, Jianjun Lei, Huazhu Fu, Junhui Hou, Qingming Huang, and Sam Kwong. Going from RGB to RGB-D saliency: A depth-guided transformation model. *IEEE TCYB*, 50(8):3627–3639, 2019. 3, 7
- [10] Runmin Cong, Jianjun Lei, Changqing Zhang, Qingming Huang, Xiaochun Cao, and Chunping Hou. Saliency detection for stereoscopic images based on depth confidence analysis and multiple cues fusion. *SPL*, 23(6):819–823, 2016. 3, 7
- [11] Alexey Dosovitskiy, Lucas Beyer, Alexander Kolesnikov, Dirk Weissenborn, Xiaohua Zhai, Thomas Unterthiner, Mostafa Dehghani, Matthias Minderer, Georg Heigold, Sylvain Gelly, Jakob Uszkoreit, and Neil Houlsby. An image is worth 16x16 words: Transformers for image recognition at scale. In *ICLR*, pages 1–22, 2021. 2
- [12] Deng-Ping Fan, Cheng Gong, Yang Cao, Bo Ren, Ming-Ming Cheng, and Ali Borji. Enhanced-alignment measure for binary foreground map evaluation. In *IJCAI*, pages 698–704, 2018. 6, 7
- [13] Deng-Ping Fan, Zheng Lin, Zhao Zhang, Menglong Zhu, and Ming-Ming Cheng. Rethinking RGB-D salient object detection: Models, data sets, and large-scale benchmarks. *TNNLS*, 32(5):2075–2089, 2021. 2, 6, 7, 8
- [14] Deng-Ping Fan, Yingjie Zhai, Ali Borji, Jufeng Yang, and Ling Shao. BBS-Net: RGB-D salient object detection with a bifurcated backbone strategy network. In *ECCV*, pages 275–292. Springer, 2020. 2, 3, 7
- [15] David Feng, Nick Barnes, Shaodi You, and Chris McCarthy. Local background enclosure for RGB-D salient object detection. In *CVPR*, pages 2343–2350, 2016. 3, 7
- [16] Keren Fu, Deng-Ping Fan, Ge-Peng Ji, Qijun Zhao, Jianbing Shen, and Ce Zhu. Siamese network for RGB-D salient object detection and beyond. *IEEE TPAMI*, 2021. 2, 3, 7
- [17] Shang-Hua Gao, Yong-Qiang Tan, Ming-Ming Cheng, Chengze Lu, Yunpeng Chen, and Shuicheng Yan. Highly efficient salient object detection with 100k parameters. In *ECCV*, pages 702–721. Springer, 2020. 2, 3, 6, 7
- [18] Jingfan Guo, Tongwei Ren, and Jia Bei. Salient object detection for RGB-D image via saliency evolution. In *ICME*, pages 1–6. IEEE, 2016. 3, 7
- [19] Junwei Han, Hao Chen, Nian Liu, Chenggang Yan, and Xuelong Li. CNNs-based RGB-D saliency detection via cross-view transfer and multiview fusion. *IEEE TCYB*, 48(11):3171–3183, 2018. 2
- [20] Kaiming He, Xiangyu Zhang, Shaoqing Ren, and Jian Sun. Deep residual learning for image recognition. In *CVPR*, pages 770–778, 2016. 2, 3
- [21] Wei Ji, Jingjing Li, Shuang Yu, Miao Zhang, Yongri Piao, Shunyu Yao, Qi Bi, Kai Ma, Yefeng Zheng, Huchuan Lu, and Li Cheng. Calibrated RGB-D salient object detection. In *CVPR*, pages 9471–9481, 2021. 2, 3
- [22] Wei Ji, Jingjing Li, Miao Zhang, Yongri Piao, and Huchuan Lu. Accurate RGB-D salient object detection via collaborative learning. In *ECCV*, pages 52–69. Springer, 2020. 7
- [23] Lai Jiang, Mai Xu, Xiaofei Wang, and Leonid Sigal. Saliency-guided image translation. In *CVPR*, pages 16509–16518, 2021. 1
- [24] Ran Ju, Ling Ge, Wenjing Geng, Tongwei Ren, and Gangshan Wu. Depth saliency based on anisotropic center-surround difference. In *ICIP*, pages 1115–1119. IEEE, 2014. 6, 7
- [25] Hyeonseok Lee and Sungchan Kim. SSPNet: Learning spatiotemporal saliency prediction networks for visual tracking. *Information Sciences*, 575:399–416, 2021. 1
- [26] Seungho Lee, Minhyun Lee, Jongwuk Lee, and Hyunjung Shim. Railroad is not a train: Saliency as pseudo-pixel su-

- pervision for weakly supervised semantic segmentation. In *CVPR*, pages 5495–5505, 2021. 1
- [27] Chongyi Li, Runmin Cong, Yongri Piao, Qianqian Xu, and Chen Change Loy. RGB-D salient object detection with cross-modality modulation and selection. In *ECCV*, pages 225–241. Springer, 2020. 7
- [28] Gongyang Li, Zhi Liu, and Haibin Ling. ICNet: Information conversion network for RGB-D based salient object detection. *IEEE TIP*, 29:4873–4884, 2020. 3, 7
- [29] Guanbin Li and Yizhou Yu. Visual saliency based on multiscale deep features. In *CVPR*, pages 5455–5463, 2015. 6, 7
- [30] Yin Li, Xiaodi Hou, Christof Koch, James M Rehg, and Alan L Yuille. The secrets of salient object segmentation. In *CVPR*, pages 280–287, 2014. 6, 7
- [31] Nian Liu, Ni Zhang, and Junwei Han. Learning selective self-mutual attention for RGB-D saliency detection. In *CVPR*, pages 13756–13765, 2020. 7
- [32] Nian Liu, Ni Zhang, Kaiyuan Wan, Ling Shao, and Junwei Han. Visual saliency transformer. In *ICCV*, pages 4722–4732, 2021. 3, 6, 7, 8
- [33] Ze Liu, Yutong Lin, Yue Cao, Han Hu, Yixuan Wei, Zheng Zhang, Stephen Lin, and Baining Guo. Swin transformer: Hierarchical vision transformer using shifted windows. In *ICCV*, pages 10012–10022, 2021. 2, 3
- [34] Zhengyi Liu, Yuan Wang, Zhengzheng Tu, Yun Xiao, and Bin Tang. TriTransNet: RGB-D salient object detection with a triplet transformer embedding network. In *ACM MM*, pages 4481–4490, 2021. 3, 6, 7, 8
- [35] Jonathan Long, Evan Shelhamer, and Trevor Darrell. Fully convolutional networks for semantic segmentation. In *CVPR*, pages 3431–3440, 2015. 4
- [36] Ao Luo, Xin Li, Fan Yang, Zhicheng Jiao, Hong Cheng, and Siwei Lyu. Cascade graph neural networks for RGB-D salient object detection. In *ECCV*, pages 346–364. Springer, 2020. 7
- [37] Yuzhen Niu, Yujie Geng, Xueqing Li, and Feng Liu. Leveraging stereopsis for saliency analysis. In *CVPR*, pages 454–461. IEEE, 2012. 6, 7
- [38] Youwei Pang, Xiaoqi Zhao, Lihe Zhang, and Huchuan Lu. Multi-scale interactive network for salient object detection. In *CVPR*, pages 9413–9422, 2020. 2, 3, 6, 7, 8
- [39] Houwen Peng, Bing Li, Weihua Xiong, Weiming Hu, and Rongrong Ji. RGB-D salient object detection: a benchmark and algorithms. In *ECCV*, pages 92–109. Springer, 2014. 6, 7, 8
- [40] Federico Perazzi, Philipp Krähenbühl, Yael Pritch, and Alexander Hornung. Saliency filters: Contrast based filtering for salient region detection. In *CVPR*, pages 733–740. IEEE, 2012. 6, 7
- [41] Yongri Piao, Wei Ji, Jingjing Li, Miao Zhang, and Huchuan Lu. Depth-induced multi-scale recurrent attention network for saliency detection. In *ICCV*, pages 7254–7263, 2019. 3
- [42] Yongri Piao, Zhengkun Rong, Miao Zhang, Weisong Ren, and Huchuan Lu. A2dele: Adaptive and attentive depth distiller for efficient RGB-D salient object detection. In *CVPR*, pages 9060–9069, 2020. 7
- [43] Aditya Prakash, Kashyap Chitta, and Andreas Geiger. Multi-modal fusion transformer for end-to-end autonomous driving. In *CVPR*, pages 7077–7087, 2021. 3, 5
- [44] Olaf Ronneberger, Philipp Fischer, and Thomas Brox. U-Net: Convolutional networks for biomedical image segmentation. In *MICCAI*, pages 234–241. Springer, 2015. 4
- [45] Olga Russakovsky, Jia Deng, Hao Su, Jonathan Krause, Sanjeev Satheesh, Sean Ma, Zhiheng Huang, Andrej Karpathy, Aditya Khosla, et al. ImageNet large scale visual recognition challenge. *IJCV*, 115(3):211–252, 2015. 6
- [46] Hualian Sheng, Sijia Cai, Yuan Liu, Bing Deng, Jianqiang Huang, Xian-Sheng Hua, and Min-Jian Zhao. Improving 3D object detection with channel-wise transformer. In *CVPR*, pages 2743–2752, 2021. 2
- [47] K. Simonyan and A. Zisserman. Very deep convolutional networks for large-scale image recognition. In *ICLR*, pages 1–14, 2015. 3
- [48] Hangke Song, Zhi Liu, Huan Du, Guangling Sun, Olivier Le Meur, and Tongwei Ren. Depth-aware salient object detection and segmentation via multiscale discriminative saliency fusion and bootstrap learning. *IEEE TIP*, 26(9):4204–4216, 2017. 3, 7
- [49] Robin Strudel, Ricardo Garcia, Ivan Laptev, and Cordelia Schmid. Segmenter: Transformer for semantic segmentation. In *ICCV*, pages 7262–7272, 2021. 2
- [50] Lv Tang, Bo Li, Yijie Zhong, Shouhong Ding, and Mofei Song. Disentangled high quality salient object detection. In *ICCV*, pages 3580–3590, 2021. 2, 3, 7
- [51] Ashish Vaswani, Noam Shazeer, Niki Parmar, Jakob Uszkoreit, Llion Jones, Aidan N Gomez, Łukasz Kaiser, and Illia Polosukhin. Attention is all you need. In *NeurIPS*, pages 5998–6008, 2017. 3
- [52] Lijun Wang, Huchuan Lu, Yifan Wang, Mengyang Feng, Dong Wang, Baocai Yin, and Xiang Ruan. Learning to detect salient objects with image-level supervision. In *CVPR*, pages 136–145, 2017. 6, 7
- [53] Yuqing Wang, Zhaoliang Xu, Xinlong Wang, Chunhua Shen, Baoshan Cheng, Hao Shen, and Huaxia Xia. End-to-end video instance segmentation with transformers. In *CVPR*, pages 8741–8750, 2021. 2
- [54] Jun Wei, Shuhui Wang, Zhe Wu, Chi Su, Qingming Huang, and Qi Tian. Label decoupling framework for salient object detection. In *CVPR*, pages 13025–13034, 2020. 2, 3, 6, 7, 8
- [55] Qiong Yan, Li Xu, Jianping Shi, and Jiaya Jia. Hierarchical saliency detection. In *CVPR*, pages 1155–1162, 2013. 6, 7
- [56] Chuan Yang, Lihe Zhang, Huchuan Lu, Xiang Ruan, and Ming-Hsuan Yang. Saliency detection via graph-based manifold ranking. In *CVPR*, pages 3166–3173, 2013. 6, 7
- [57] Li Yuan, Yunpeng Chen, Tao Wang, Weihao Yu, Yujun Shi, Zi-Hang Jiang, Francis E.H. Tay, Jiashi Feng, and Shuicheng Yan. Tokens-to-Token ViT: Training vision transformers from scratch on ImageNet. In *ICCV*, pages 558–567, 2021. 2, 3
- [58] Hao Zhang, Yanbin Hao, and Chong-Wah Ngo. Token shift transformer for video classification. In *ACM MM*, pages 917–925, 2021. 2

- [59] Jing Zhang, Deng-Ping Fan, Yuchao Dai, Saeed Anwar, Fatemeh Saleh, Sadegh Aliakbarian, and Nick Barnes. Uncertainty inspired RGB-D saliency detection. *IEEE TPAMI*, 2021. 3, 7
- [60] Miao Zhang, Weisong Ren, Yongri Piao, Zhengkun Rong, and Huchuan Lu. Select, supplement and focus for RGB-D saliency detection. In *CVPR*, pages 3472–3481, 2020. 7
- [61] Wenbo Zhang, Ge-Peng Ji, Zhuo Wang, Keren Fu, and Qijun Zhao. Depth quality-inspired feature manipulation for efficient RGB-D salient object detection. In *ACM MM*, pages 731–740, 2021. 2, 7, 8
- [62] Wenbo Zhang, Yao Jiang, Keren Fu, and Qijun Zhao. BTS-Net: Bi-directional transfer-and-selection network for RGB-D salient object detection. In *ICME*, pages 1–6. IEEE, 2021. 2, 3, 7, 8
- [63] Jiawei Zhao, Yifan Zhao, Jia Li, and Xiaowu Chen. Is depth really necessary for salient object detection? In *ACM MM*, pages 1745–1754, 2020. 1, 2, 3, 5, 6, 7, 8
- [64] Jia-Xing Zhao, Yang Cao, Deng-Ping Fan, Ming-Ming Cheng, Xuan-Yi Li, and Le Zhang. Contrast prior and fluid pyramid integration for RGB-D salient object detection. In *CVPR*, pages 3927–3936, 2019. 2, 3
- [65] Liming Zhao, Mingjie Li, Depu Meng, Xi Li, Zhaoxiang Zhang, Yueting Zhuang, Zhuowen Tu, and Jingdong Wang. Deep convolutional neural networks with merge-and-run mappings. In *IJCAI*, page 3170–3176, 2018. 2
- [66] Ting Zhao and Xiangqian Wu. Pyramid feature attention network for saliency detection. In *CVPR*, pages 3085–3094, 2019. 1
- [67] Xiaoqi Zhao, Youwei Pang, Lihe Zhang, Huchuan Lu, and Lei Zhang. Suppress and balance: A simple gated network for salient object detection. In *ECCV*, pages 35–51. Springer, 2020. 2, 3, 6, 7, 8
- [68] Xiaoqi Zhao, Lihe Zhang, Youwei Pang, Huchuan Lu, and Lei Zhang. A single stream network for robust and real-time RGB-D salient object detection. In *ECCV*, pages 646–662. Springer, 2020. 2, 7
- [69] Sixiao Zheng, Jiachen Lu, Hengshuang Zhao, Xiatian Zhu, Zekun Luo, Yabiao Wang, Yanwei Fu, Jianfeng Feng, Tao Xiang, Philip HS Torr, et al. Rethinking semantic segmentation from a sequence-to-sequence perspective with transformers. In *CVPR*, pages 6881–6890, 2021. 2
- [70] Huajun Zhou, Xiaohua Xie, Jian-Huang Lai, Zixuan Chen, and Lingxiao Yang. Interactive two-stream decoder for accurate and fast saliency detection. In *CVPR*, pages 9141–9150, 2020. 6, 7, 8
- [71] Chunbiao Zhu and Ge Li. A three-pathway psychobiological framework of salient object detection using stereoscopic technology. In *ICCVW*, pages 3008–3014, 2017. 6, 7
- [72] Chunbiao Zhu, Ge Li, Wenmin Wang, and Ronggang Wang. An innovative salient object detection using center-dark channel prior. In *ICCVW*, pages 1509–1515, 2017. 3, 7